

Coherent single-spin control with high-fidelity singlet-triplet readout in silicon

R. Zhao,^{1,*} T. Tantt,¹ K. Y. Tan,² B. Hensen,¹ K. W. Chan,^{1,†} J. C. C. Hwang,^{1,‡} R. C. C. Leon,¹ C. H. Yang,¹ W. Gilbert,¹ F. E. Hudson,¹ K. M. Itoh,³ A. A. Kiselev,⁴ T. D. Ladd,⁴ A. Morello,¹ A. Laucht,¹ and A. S. Dzurak¹

¹*Centre for Quantum Computation & Communication Technology,
School of Electrical Engineering & Telecommunications,*

University of New South Wales, Sydney, New South Wales 2052, Australia

²*QCD Labs, COMP Centre of Excellence, Department of Applied Physics, Aalto University, 00076 AALTO, Finland*

³*School of Fundamental Science and Technology, Keio University,
3-14-1 Hiyoshi, Kohoku-ku, Yokohama 223-8522, Japan*

⁴*HRL Laboratories, LLC, 3011 Malibu Canyon Rd., Malibu, CA 90265, USA*

(Dated: March 25, 2025)

Single electron spins in silicon can be used to realize quantum bits (qubits) that profit from the long coherence times inherent to the host material¹⁻⁴. When confined in quantum dots (QDs) using electrostatic gates, there is the added promise of scalability by leveraging industrial semiconductor manufacturing technology⁵⁻⁸. However, most single-electron spin qubits produced to date employ quantum state readout via spin-dependent-tunnelling to an electron reservoir⁹. This requires significant on-chip real estate, limiting the prospects for large scale multi-qubit systems. Here, we address this challenge by combining coherent single-spin control with high-fidelity, single-shot, singlet-triplet readout. We employ Pauli spin blockade in a double QDs as a readout tool to achieve a measurement fidelity of 99.3 %. This allows us to implement coherent electron spin resonance (ESR) control at magnetic fields as low as 150 mT, corresponding to a carrier frequency of 4.2 GHz, eliminating the need for high-frequency microwave sources. We discover that the qubits decohere faster at low magnetic fields with $T_2^{\text{Rabi}} = 18.6 \mu\text{s}$ and $T_2^* = 1.4 \mu\text{s}$ at 150 mT. Their coherence is limited by spin flips of residual ²⁹Si nuclei in the isotopically enriched ²⁸Si host material, that occur more frequently at lower fields. Our finding highlights the importance of further isotopic enrichment of device substrates for the realization of a scalable silicon-based quantum processor.

The rapid progress of spin qubits in silicon QDs has been fuelled by coherent electron spin resonance (ESR), either driven by an ac magnetic³ or electric-field^{10,11}. To date, ESR has enabled the demonstration of high-fidelity single- and two-qubit logic gates approaching the fault tolerance threshold¹²⁻¹⁷. In most of these demonstrations, single-shot spin readout was performed via spin-selective tunnelling of a single spin to a reservoir⁹, however this technique is problematic for the operation of large-scale multi-qubit architectures^{6,18}. In order to work, it would require complex, coherent single-spin shuttling^{19,20} or a chain of swap gate opera-

tions²¹ to readout qubits distant from a reservoir. Furthermore, quantum error correction protocols require simultaneous spin-state readout at arbitrary locations in the large-scale qubit array¹⁸. The preferred method for spin-readout is, therefore, singlet-triplet (ST) readout via Pauli spin blockade (PSB) in a double QDs system²². Besides alleviating the design constraints imposed by reservoir readout, single-shot dispersive ST readout can also leverage state-of-the-art reflectometry technology to enable gate-based sensors with extremely small on-chip footprint²³⁻²⁵. Furthermore, ST readout forms the foundation of parity measurements, a main ingredient of many quantum error correction protocols¹⁸, and does not require the Zeeman splitting energy to be much larger than the thermal energy, which is a limiting constraint with reservoir-based readout⁹. It therefore constitutes a robust readout technique that allows qubit operation over a wide range of magnetic fields. Low magnetic fields, in particular, are highly desirable because they enable qubit operation at lower spin resonance frequencies, simplifying microwave engineering and requiring less expensive signal generators. Coherent ESR and high-fidelity ST readout are therefore the key elements for the implementation of a scalable, silicon-based quantum processor^{6,18}. Previous experiments have shown the compatibility of these two techniques for electrons in GaAs^{26,27}, however in silicon, demonstrations using electron spins have so far remained incoherent²¹, while those employing hole spins are yet to achieve single-shot readout²⁸.

In this work, we achieve coherent, single-electron spin control with high-fidelity ST readout at a dc magnetic field of 150 mT. The device consists of a linear array of silicon metal-oxide-semiconductor (Si-MOS) QDs, electrostatically defined by a palladium (Pd) gate stack²⁹ on an isotopically enriched ²⁸Si epi-layer³⁰ (see Methods section). Fig. 1a shows a false-coloured scanning electron micrograph of a device nominally identical to the one used in this study. A cross-sectional schematic is plotted in Fig. 1b. We have labelled the QD accumulation gates (G1-G6), the confinement gate (CB) that confines the QDs laterally, the reservoir gate (RG) that accumulates the electron reservoir for loading and unloading electrons, the single-electron transistor (SET)

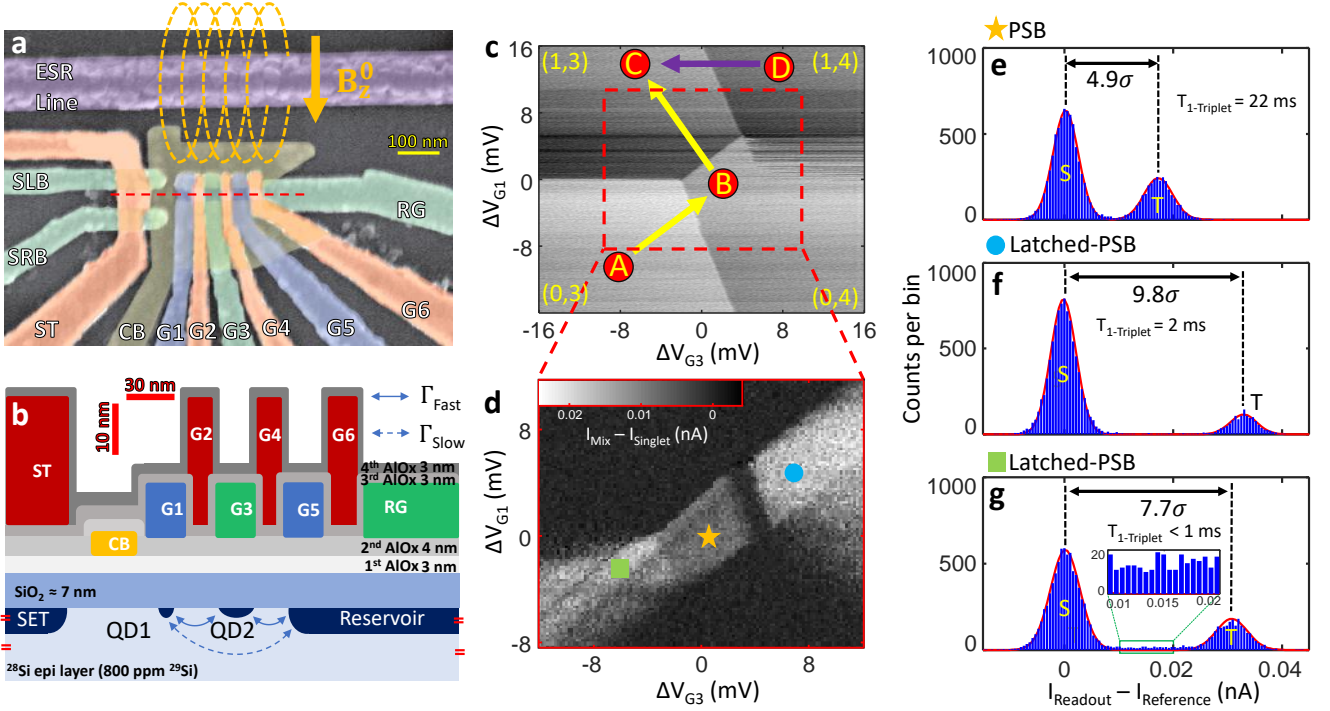


Figure 1 | Device layout and high-fidelity singlet-triplet readout. **a**, False-coloured scanning electron micrograph of an identical device. The orange arrow indicates the direction of the dc magnetic field B_z^0 , which is aligned in plane to minimize spin-orbit coupling and reduce the qubits' sensitivity to charge noise. **b**, Cross-sectional schematic along the red dashed line in **a**, showing the Pd gate stack with insulating atomic-layer-deposited aluminium oxide layers. **c**, Charge stability map around the (1,3) - (0,4) anti-crossing. The pulse sequence A-B-C (yellow arrows) prepares a separated double dot with electrons in the singlet state, while the pulse sequence D-C (blue arrow) prepares the double dot in a mixed state. The pulse sequence C-B facilitates the spin readout operation by attempting to push the electron from QD1 into QD2. Tunnelling will occur if the electron in QD1 forms a singlet with the electron in QD2, but it is blocked if the electrons form a triplet. **d**, Difference in SET current between singlet and mixed spin state preparation, plotted as a function of the two gate voltages ΔV_{G1} and ΔV_{G3} . Apparent are the regions of standard PSB (star) and enhanced latching readout (circle, square). **e-g**, Histograms of the SET current signal for 10200 single-shot readouts with 120 μ s integration time and 5 pA bin width, using the **e**, standard PSB, or **f,g**, enhanced latching readout regions as indicated by the coloured markers in **d**.

charge sensor (ST, SLB, SRB), and the short of the broadband ESR antenna to apply MW pulses³¹ for spin control.

When tuning up the device, we use the following procedure to find the PSB region that gives us high-fidelity, single-shot ST readout. First, we carefully tune all the gate voltages to accumulate two QDs at the approximate locations indicated in Fig. 1b, using the charge sensing technique described in Ref. 32. We then choose the (1,3) - (0,4) anti-crossing, shown in Fig. 1c, as our working point. We assume the first two electrons in QD2 to form a singlet and not to interact with the third and fourth electrons during the experiment. Second, we either initialize the two QDs in a singlet state or in a mixed state of singlet and triplet. When pulsing from point A to point B (yellow arrow) we load a fourth electron on QD2, with the last two electrons forming an anti-parallel spin pair (singlet). Further pulsing to point C will separate these two electrons across the two QDs,

keeping them in the singlet state. Alternatively, when pulsing from point D to C, we will randomly remove one of the four electrons from QD2. The spin of the remaining, third electron could be either anti-parallel or parallel with the spin in QD1, leaving the two QDs initialized in a mix of triplet and singlet. Third, we find the region of PSB, by alternately initializing a singlet and a mixed state, and pulsing to a point around the (1,3) - (0,4) anti-crossing. Fig. 1d plots the difference in the SET current for the two different initializations, performed interleaved to reject slow drifts of the charge sensor. When the two QDs are in the singlet state, the single electron in QD1 can tunnel onto QD2 causing a change in charge configuration from (1,3) to (0,4). However, when they are in the triplet state, tunnelling is inhibited by PSB and the system remains in the (1,3) charge configuration²². Therefore, initialization into the mixed state will result in some probability for the charge sensor giving a reading that represents a triplet. We detect

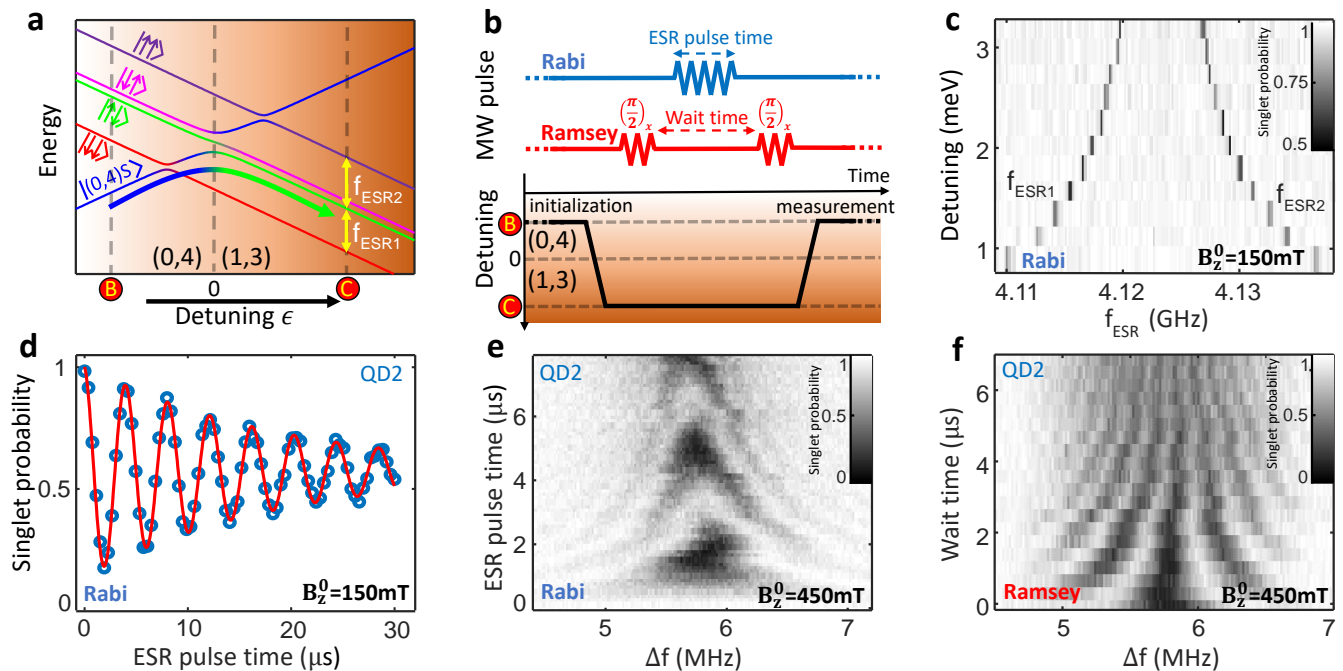


Figure 2 | Coherent single-spin control with ST readout. **a**, Schematic energy level diagram of the (1,3) - (0,4) anticrossing. **b**, Partial pulse sequences for the coherent spin control experiments in **d-f**. The sequences start with initializing the system in the (0,4)S state by pulsing from point A to point B (see Fig. 1c). Then we prepare a $|\uparrow\downarrow\rangle$ by moving from point B to point C. As indicated by the curved colour-graded arrow, we pulse diabatically across the S-T⁻ anti-crossing, but adiabatically with respect to all the other anti-crossings. We then apply the microwave control pulses at the deep detuning point C to manipulate the individual spins. After spin manipulation, we perform readout by converting $|\uparrow\downarrow\rangle$ and $|\downarrow\uparrow\rangle$ into triplet, by pulsing from point C back to the standard PSB region B. The $|\downarrow\uparrow\rangle$ state is not accessed during this measurement. **c**, The two ESR peaks plotted as a function of detuning ϵ . We use an incoherent ESR pulse of 100 μ s for this experiment. We identify the lower (higher) frequency peak corresponding to the QD1 (QD2) through the Stark-shift measurements described in Ref. 3. **d-f**, Coherent spin control of QD2 showing **d**, Rabi oscillations, **e**, Rabi chevron, and **f**, Ramsey fringes. We use frequency mixing to implement the ESR pulse scheme. Δf is the difference between the output and the carrier frequencies of the microwave source.

a clear standard PSB region and two enhanced latching regions, in which the very different tunnelling times from the two QDs to the reservoir are used to cause a state dependent change in total charge³³.

We have designed the orientation of the SET to maximize its sensitivity to inter-dot charge tunnelling events, and achieve good signal contrast for ST readout. As shown in the SET current histogram in Fig. 1e, the signal peaks for standard PSB are separated by 4.9σ , indicating a charge state readout fidelity $> 99.8 \%$. The enhanced latching readout mechanism further increases the signal contrast between the singlet and triplet state, up to 9.8σ (see Fig. 1f,g). Such good contrast would allow charge readout with $< 0.005 \%$ error, however we find the latched meta state lifetime to be 2 ms or shorter. This is only one order of magnitude slower than the 120 μ s integration time that is required to achieve good signal separation for our experimental setup. Consequently, we notice a non-zero background between the singlet and triplet peaks in Fig. 1g, evidencing decay from the triplet state to the singlet state during measurement. To avoid the spin readout error caused by

the latched meta state relaxation as well as mapping errors³³, we chose the standard PSB region for readout. The triplet lifetime for standard PSB is 22 ms, which results in a $\sim 0.5 \%$ spin to charge conversion error. This reduces the total fidelity of the single-shot ST readout using standard PSB to 99.3%. The latched metastate lifetime could be improved in future experiments by defining a third electron under G5 to fine-tune the electron tunnelling rate from QD1 and QD2 to the reservoir³⁵.

In this study, we control the spins of the electrons using an ac magnetic field generated by the on-chip microwave antenna³¹. In Fig. 2a we plot a schematic of the energy level diagram as a function of energy detuning ϵ and in Fig. 2b the pulse sequences that we used to achieve ESR. As shown in Fig. 2c for $B_z^0 = 150$ mT, we find two resonance peaks that correspond to rotations of QD1 (lower frequency) and QD2 (higher frequency). When we decrease ϵ , the splitting between the two peaks increases, denoting the larger exchange coupling J between the electrons and mapping out the energy structure of the (1,3) - (0,4) anticrossing in the shallow

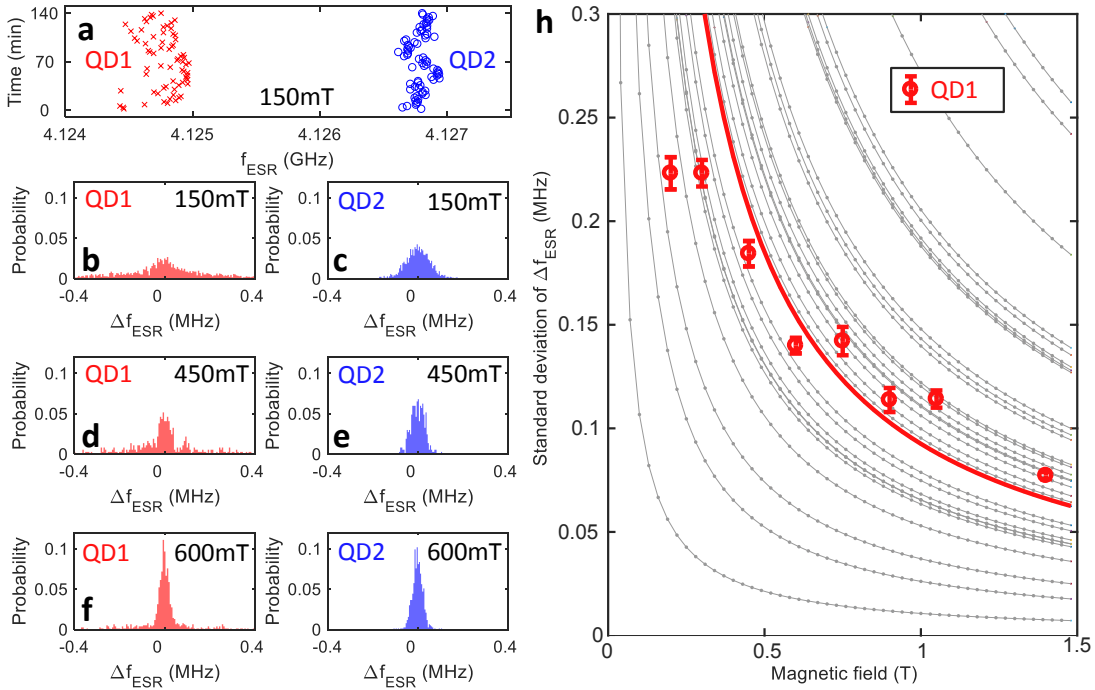


Figure 3 | ^{29}Si -induced ESR frequency fluctuations. **a**, Measurement of ESR frequencies of the two qubits over a time period of 140 mins at 150 mT. There are significant fluctuations of the ESR frequencies of both qubits. Each point of measurement lasts about 2 mins. **b-g**, Histograms of ESR frequency fluctuations for both qubits at various magnetic fields. The distribution becomes more concentrated at higher magnetic field. **h**, Red circles show the standard deviation of the fluctuation in ESR frequency of qubit QD1 plotted as a function of magnetic field, with error bars derived as in Ref. 34. Each point is calculated based on a measurement that lasts 8 hours. The red line is a fit $\propto 1/B_z^0$. Small gray points, each with gray lines $\propto 1/B_z^0$, indicate simulations of ^{29}Si nuclear spin-flip processes for 30 simulated samples with random nuclear placements. The error bars correspond to the standard error of the sample standard deviation estimated from the raw ESR jump data without any assumptions of the shape of the underlying distribution.

detuning region. Next, we investigate the coherence of the spin qubits in low magnetic fields. By varying the ESR pulse time, we observe clear Rabi oscillations (Fig. 2d) at a magnetic field as low as $B_z^0 = 150$ mT, with $T_2^{\text{Rabi}} = 18.6$ μs . In Fig. 2e, we plot the Rabi chevron for one of the qubits at $B_z^0 = 450$ mT. We also use a Ramsey sequence (Fig. 2f) to measure T_2^* at various magnetic fields. The observed T_2^* values are reported in Table I.

The ability to perform coherent control on the spin states allows us to experimentally validate the combined initialization, control and measurement fidelity. We extract the maximum readout visibility for the $|\uparrow\uparrow\rangle$ state by fitting the Rabi oscillations in Fig. 2d. The maximum visibility is 87.1 ± 1.9 %, which is noticeably lower

B_z^0 (mT)	150	300	450
f_{Rabi} (MHz)	0.25	0.25	0.33
T_2^* (μs)	1.4 ± 0.21	2.5 ± 0.3	3.3 ± 0.65

TABLE I | Observed T_2^* at three different magnetic fields B_z^0 with its associated Rabi frequencies f_{Rabi} .

than our earlier estimate of the readout fidelity. During this measurement campaign, we observed frequent jumps in the ESR frequencies of both qubits due to spin flip of the surrounding ^{29}Si nuclei. This renders it difficult to keep the microwave frequency exactly on-resonance for the duration of the measurement (see also Fig. 2e). Therefore, the true readout visibility of the $|\uparrow\uparrow\rangle$ state may not be reflected in this measurement. We also studied the maximum readout visibility for the three other spin states ($|\downarrow\uparrow\rangle$, $|\uparrow\downarrow\rangle$ and $|\downarrow\downarrow\rangle$) using complementary measurements. The visibility for $|\uparrow\downarrow\rangle$ is as high as 99.5 ± 0.7 %, consistent with the readout fidelity estimated previously. The results are summarized in Table II with more details given in the Extended Data Fig. 1 and Supplementary Information.

The robustness of ST readout allows us to employ tracking of the ESR frequency as a tool to study the nuclear spin environment of the spin qubits over a wide range of magnetic fields from $B_z^0 = 150$ mT to 1.4 T. As already noticeable in Fig. 2e, we observe fluctuations of the ESR frequencies $\Delta f_{\text{ESR}} = f_{\text{ESR}}(t_2) - f_{\text{ESR}}(t_1)$ of both qubits in time. More detailed data is shown in Fig. 3a, where we track the ESR frequencies of both qubits over 140 mins. There is no correlation between

Spin state	Readout outcome	Visibility	Method	Limitation
$ \uparrow\uparrow\rangle$	Triplet	$87\pm 1.9\%$	ESR driven $ \uparrow\uparrow\rangle \Leftrightarrow \uparrow\downarrow\rangle$ oscillation	Control
$ \downarrow\uparrow\rangle$	Triplet	$99.3\pm 2.3\%$	Exchange driven $ \downarrow\uparrow\rangle \Leftrightarrow \uparrow\downarrow\rangle$ oscillation	Readout
$ \uparrow\downarrow\rangle$	Singlet	$99.5\pm 0.7\%$	$ \uparrow\downarrow\rangle \Rightarrow \downarrow\downarrow\rangle$ T_1 relaxation	Readout
$ \downarrow\downarrow\rangle$	Triplet	$96.8\pm 1.0\%$	$ \uparrow\downarrow\rangle \Rightarrow \downarrow\downarrow\rangle$ T_1 relaxation	Thermalization

TABLE II | Maximum readout visibility for the four spin states of the two-qubit system. The error bar for $|\uparrow\uparrow\rangle$ state visibility is derived from the fit of ESR driven Rabi oscillations shown in Fig 2d. Similarly, the fit of exchange-driven Rabi oscillations shown in Fig. 1(c) gives the error bar for $|\downarrow\uparrow\rangle$ state visibility. The exchange driven $|\downarrow\uparrow\rangle \Leftrightarrow |\uparrow\downarrow\rangle$ oscillation experiment is reported in the Extended Data Fig. 1. The errors for $|\uparrow\downarrow\rangle$ and $|\downarrow\downarrow\rangle$ state visibility are derived from the fit of the exponential decay curve between the two states as reported in the Supplementary Information.

$\Delta f_{\text{ESR}}^{\text{QD1}}$ and $\Delta f_{\text{ESR}}^{\text{QD2}}$, indicating that any fluctuations are caused by a highly localized effect. We postulate the fluctuations in ESR frequency to be caused by the residual (800 ppm) ^{29}Si nuclear spins in the isotopically enriched substrate. Similar observations were already published in Ref. 15 on a different device. Figs. 3b-g show the histograms of Δf_{ESR} at three different magnetic fields for both qubits. We observe that the distribution of Δf_{ESR} becomes narrower as the magnetic field increases. To better quantify this effect, we plot the standard deviation of $\Delta f_{\text{ESR}}^{\text{QD1}}$ as a function of magnetic field in Fig. 3h and compare it to numerical models for the hyperfine-interaction during electron singlet initialization, ESR drive, and ST measurement. These models indicate that nuclei are largely driven by the microwave ESR drive in conjunction with the anisotropic hyperfine interaction, while other contributions such as “ionization shock” from electron tunneling are negligible. Details of these conclusions and this model may be found in the supplementary material. Furthermore, these numeric simulations indicate that with 800 ppm ^{29}Si , the total amount of ESR-driven nuclear spin noise can easily vary by two orders of magnitude depending on the particular placement of the nuclear spins relative to the dot. Figure 3h shows traces for 30 simulated quantum dots each with random ^{29}Si placement, illustrating this variation. At low magnetic fields, reducing ESR frequency drift due to nuclear fluctuations may require additional isotopic purification.

In summary, we have successfully operated spin qubits in a silicon platform with a readout fidelity higher than 99.3 %. The ST readout scheme enables coherent control of single spins at a magnetic field of 150 mT and a resonance frequency as low as 4.1 GHz. Such lower-frequency qubit operation significantly improves the scalability prospects for future silicon quantum processors. In addition, the ST readout technique has enabled a more detailed study of important effects in magnetic noise, which becomes more profound when silicon qubits are operated in such a low magnetic field environment. Despite using an isotopically enriched ^{28}Si substrate, there remain residual ^{29}Si nuclear spins located in the vicinity of the qubits, causing fluctuations in the qubit operation frequencies. We observe

the nuclear spin flip rate to increase as the applied external magnetic field decreases, an effect that can be reduced in future devices by increasing the ^{28}Si isotopic enrichment.

METHODS

Figs. 1a and b show a scanning electron micrograph and a cross-sectional schematic of the sample used in this study. It is fabricated on top of a 900 nm thick, isotopically enriched ^{28}Si epi-layer with 800 ppm residual ^{29}Si on a natural silicon substrate³⁰. We first grow a 7 nm thick thermal SiO_2 plus a 3 nm atomic layer deposition (ALD) aluminium oxide to prevent gate to substrate leakage. Then, we use electron-beam lithography to write the nanoscale gate pattern and perform resist development in pre-cooled (-20°C) Methyl Isobutyl Ketone solution with ultrasound agitation. In the next step, we evaporate Pd onto the chip to form the gate electrodes. Since Pd has a much smaller grain size than aluminium, we routinely achieve gate features as narrow as 12 nm. A 2 nm thin Titanium (Ti) layer is evaporated prior to Pd deposition to enhance the cohesion of the Pd gate onto the oxide. The above lithography process is repeated several times to form the stack of Pd gate electrodes. Since Pd does not have a native oxide, we use ALD to grow 3-4 nm aluminium oxide on top of the gates to provide electrical insulation between different layers. Lastly, the sample is annealed in forming gas at 400°C for 15 mins to repair the damage caused by lithography.

Stanford Research Systems SIM928 modular programmable voltage sources are used to dc-bias all gate electrodes shown in Fig. 1a and b. In addition, voltage pulses from an arbitrary waveform generator (Tektronix AWG7122) are applied to G1 and G3 through a voltage combiner. The bandwidth for dc bias (ac pulses) is 30 Hz (80 MHz). We use a nanoscale on-chip integrated 40-GHz antenna to generate the ac magnetic field to drive the electron spin resonance³¹. The antenna is powered by a vector microwave source (Agilent E8267D PSG). The sample is cooled down in an Oxford Instruments, liquid-helium cooled, dilution

refrigerator with magnet. All measurements are performed at the phonon bath temperature of 37 mK.

ACKNOWLEDGMENTS

We thank W. Huang for enlightening discussions and A. Saraiva for helpful comments on the ^{29}Si nuclear spin modeling. We acknowledge support from the Australian Research Council (CE170100012), the US Army Research Office (W911NF-17-10198) and the NSW Node of the Australian National Fabrication Facility. The views and conclusions contained in this document are those of the authors and should not be interpreted as representing the official policies, either expressed or im-

plied, of the Army Research Office or the U.S. Government. The U.S. Government is authorized to reproduce and distribute reprints for Government purposes notwithstanding any copyright notation herein. B.H. acknowledges support from the Netherlands Organization for Scientific Research (NWO) through a Rubicon Grant. K.M.I. acknowledges support from a Grant-in-Aid for Scientific Research by MEXT, NanoQuine, FIRST, and the JSPS Core-to-Core Program.

AUTHOR INFORMATION

The authors declare no competing financial interests. Readers are welcome to comment on the online version of the paper. Correspondence and request for materials should be addressed to R.Z. (ruichen77@gmail.com) or A.S.D. (a.dzurak@unsw.edu.au).

* Present address: National Institute of Standards and Technology, 325 Broadway, Boulder, CO 80305, United States.

† Present address: Microsoft Quantum, The University of Sydney, Sydney, NSW 2006, Australia.

‡ Present address: Research and Prototype Foundry, The University of Sydney, Sydney, NSW 2006, Australia.

¹ A. M. Tyryshkin *et al.*, *Nature materials* **11**, 143 (2012).

² J. T. Muhonen *et al.*, *Nature Nanotechnology* **9**, 986 (2014).

³ M. Veldhorst *et al.*, *Nature Nanotechnology* **9**, 981 (2014).

⁴ T. D. Ladd and M. S. C., *Encyclopedia of Modern Optics (Second Edition)*, 467 (2018).

⁵ R. Maurand *et al.*, *Nature Communications* **7**, 13575 (2016).

⁶ M. Veldhorst, H. G. J. Eenink, C. H. Yang, and A. S. Dzurak, *Nature communications* **8**, 1766 (2017).

⁷ L. Hutin *et al.*, in *2018 48th European Solid-State Device Research Conference (ESSDERC)* (2018) pp. 12–17.

⁸ L. Vandersypen, H. Bluhm, J. Clarke, A. Dzurak, R. Ishihara, A. Morello, D. Reilly, L. Schreiber, and M. Veldhorst, *npj Quantum Information* **3**, 34 (2017).

⁹ J. M. Elzerman *et al.*, *nature* **430**, 431 (2004).

¹⁰ E. Kawakami, P. Scarlino, D. R. Ward, F. Braakman, D. Savage, M. Lagally, M. Friesen, S. N. Coppersmith, M. A. Eriksson, and L. Vandersypen, *Nature nanotechnology* **9**, 666 (2014).

¹¹ K. Takeda, J. Kamioka, T. Otsuka, J. Yoneda, T. Nakajima, M. R. Delbecq, S. Amaha, G. Allison, T. Kodera, S. Oda, *et al.*, *Science advances* **2**, e1600694 (2016).

¹² T. Watson, S. Philips, E. Kawakami, D. Ward, P. Scarlino, M. Veldhorst, D. Savage, M. Lagally, M. Friesen, S. Coppersmith, *et al.*, *Nature* **555**, 633 (2018).

¹³ D. M. Zajac *et al.*, *Science* **359**, 439 (2018).

¹⁴ J. Yoneda *et al.*, *Nature nanotechnology* **13**, 102 (2018).

¹⁵ W. Huang *et al.*, arXiv preprint arXiv:1805.05027 (2018).

¹⁶ C. H. Yang *et al.*, arXiv preprint arXiv:1807.09500 (2018).

¹⁷ X. Xue, T. Watson, J. Helsen, D. Ward, D. Savage, M. Lagally, S. Coppersmith, M. Eriksson, S. Wehner, and L. Vandersypen, arXiv preprint arXiv:1811.04002 (2018).

¹⁸ C. Jones *et al.*, *Physical Review X* **8**, 021058 (2018).

¹⁹ T. A. Baart, M. Shafiei, T. Fujita, C. Reichl, W. Wegscheider, and L. M. K. Vandersypen, *Nature nanotechnology* **11**, 330 (2016).

²⁰ T. Fujita, T. A. Baart, C. Reichl, W. Wegscheider, and L. M. K. Vandersypen, *npj Quantum Information* **3**, 22 (2017).

²¹ M. A. Fogarty *et al.*, *Nature communications* **9**, 4370 (2018).

²² A. C. Johnson, J. R. Petta, C. M. Marcus, M. P. Hanson, and A. C. Gossard, *Phys. Rev. B* **72**, 165308 (2005).

²³ W. A. *et al.*, *Nature Nanotechnology*, 1 (2019).

²⁴ P. Pakkiam, A. V. Timofeev, M. G. House, M. R. Hogg, T. Kobayashi, M. Koch, S. Rogge, and M. Y. Simmons, *Phys. Rev. X* **8**, 041032 (2018).

²⁵ M. Urdampilleta *et al.*, arXiv preprint arXiv:1809.04584 (2018).

²⁶ M. Pioro-Ladriere, T. Obata, Y. Tokura, Y.-S. Shin, T. Kubo, K. Yoshida, T. Taniyama, and S. Tarucha, *Nature Physics* **4**, 776 (2008).

²⁷ T. Ito *et al.*, arXiv preprint arXiv:1805.06111 (2018).

²⁸ A. Crippa, R. Ezzouch, A. Aprá, A. Amisse, L. Houtin, B. Bertrand, M. Vinet, M. Urdampilleta, T. Meunier, M. Sanquer, *et al.*, arXiv preprint arXiv:1811.04414 (2018).

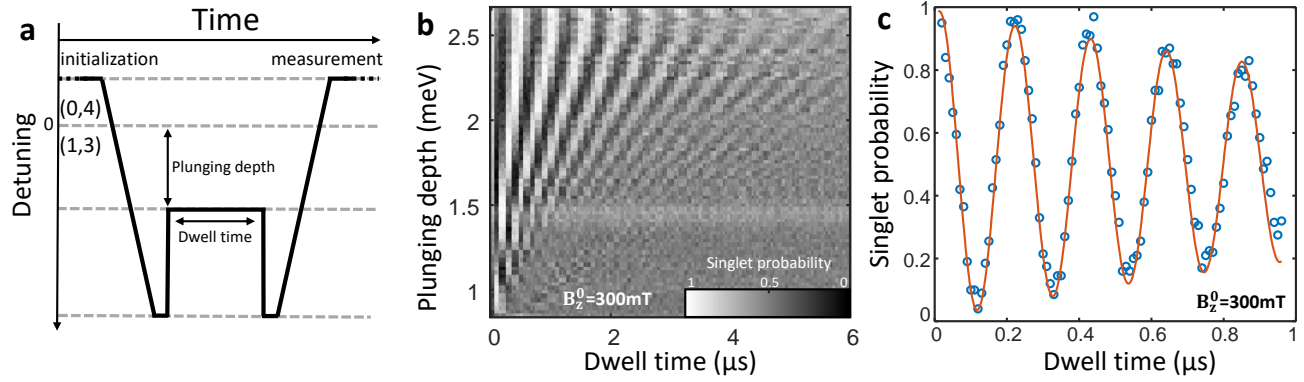
²⁹ M. Brauns, S. V. Amitonov, P. Spruijtenburg, and F. A. Zwanenburg, *Scientific reports* **8**, 5690 (2018).

³⁰ K. M. Itoh and H. Watanabe, *MRS Communications* **4**, 143157 (2014).

³¹ J. P. Dehollain, J. J. Pla, E. Siew, K. Y. Tan, A. S. Dzurak, and A. Morello, *Nanotechnology* **24**, 015202 (2012).

³² C. H. Yang, W. H. Lim, F. A. Zwanenburg, and A. S. Dzurak, *AIP Advances* **1**, 042111 (2011).

³³ P. Harvey-Collard *et al.*, *Physical Review X* **8**, 021046 (2018).



Extended Data Figure 1 | Exchange driven oscillations. **a** Schematic diagram of the pulse sequence to measure the exchange oscillations. First, we initialize the double quantum dots (DQDs) in the $|\uparrow\downarrow\rangle$ state as described in Fig. 2a. Second, we enable the exchange coupling between the two dots by pulsing to the shallow detuning region. This will drive the coherent oscillations between the $|\uparrow\downarrow\rangle$ and $|\downarrow\uparrow\rangle$ states. We then stop the exchange driven oscillations by pulsing back to the deep detuning region. Finally, another adiabatic pulse brings the DQDs from (1,3) back to (0,4) region and completes the spin measurement, during which the $|\uparrow\downarrow\rangle$ state is converted to singlet and the $|\downarrow\uparrow\rangle$ state is converted to triplet. **b** Singlet probability plotted as a function of plunging depth and dwell time at the shallow detuning region. **c** A single trace of exchange driven oscillation with plunging depths of 1.9 meV. The red solid line indicates is a fit to the Rabi's formula with maximum visibility of 99.3 ± 2.3 %.

³⁴ C. R. Rao and M. Statistiker, *Linear statistical inference and its applications*, Vol. 2 (Wiley New York, 1973).

³⁵ T. Nakajima *et al.*, Physical review letters **119**, 017701 (2017).